AIAA 2001 – 0671

A Combined Experimental/Computational Investigation of a Rocket Based Combined Cycle Inlet

Michael K. Smart
Lockheed Martin Engineering and Sciences
NASA Langley Research Center

Carl A. Trexler
Hypersonic Airbreathing Propulsion Branch
NASA Langley Research Center

Allen L. Goldman
Boeing – Rocketdyne Propulsion and Power

39th AIAA Aerospace Sciences Meeting & Exhibit
January 8-11, 2001 Reno, NV

A Combined Experimental/Computational Investigation of a Rocket Based Combined Cycle Inlet

Michael K. Smart
Aeronautical Engineer
Lockheed Martin Engineering and Sciences
NASA Langley Research Center,
MS 168, Hampton VA 23681.

Carl A. Trexler
Aerospace Engineer
Hypersonic Airbreathing Propulsion Branch
NASA Langley Research Center
MS 168, Hampton VA 23601.

Allen L. Goldman
Technical Fellow
Boeing - Rocketdyne Propulsion and Power
Mail Code IB07, 6633 Canoga Avenue
Canoga Park, CA 91303.

Abstract

A rocket based combined cycle inlet geometry has undergone wind tunnel testing and computational analysis with Mach 4 flow at the inlet face. Performance parameters obtained from the wind tunnel tests were the mass capture, the maximum back-pressure, and the self-starting characteristics of the inlet. The CFD analysis supplied a confirmation of the mass capture, the inlet efficiency and the details of the flowfield structure. Physical parameters varied during the test program were cowl geometry, cowl position, body-side bleed magnitude and ingested boundary layer thickness. An optimum configuration was determined for the inlet as a result of this work.

Nomenclature

A_{cov}	coverage area of the cowl upstream of the inlet throat
A_{fm}	flow meter throat area
A_{tot}	total spill area of the inlet upstream of the throat
h_{cowl}	cowl height
M	Mach number
$\dot{m}$	mass flow
m_{bl}	bleed mass ratio = $\dot{m}_{bl} / \dot{m}_{base}$
m_c	mass capture ratio = $\dot{m}_{cap} / \dot{m}_{base}$
p	pressure
P_T	inlet total pressure recovery
R	gas constant = 287.035 J/kg-K
t	time
T	temperature
x	axial position
x_c	distance of cowl leading edge (or crotch) upstream of the inlet throat.
δ	boundary layer thickness
δ^*	displacement thickness
γ	ratio of specific heats = 1.40
η_{KD}	inlet process efficiency
η_{KE}	inlet kinetic energy efficiency

Subscripts

1	tunnel freestream conditions
base	base-line inlet configuration
bl	bleed
cap	inlet capture
ref	reference condition
t	stagnation conditions
th	throat
w	wall

Introduction

The rocket based combined cycle (RBCC) engine concept is an attempt to combine the high thrust-to-weight of a rocket with the high specific impulse of a dual-mode scramjet. These engines usually involve the integration of a rocket within a scramjet flow path, with the rocket and scramjet providing thrust at different stages of the vehicle trajectory. A typical RBCC powered vehicle trajectory might involve air-augmented rocket operation from take-off to Mach 3-4, ramjet operation up to Mach 6-7, followed by transition to scramjet operation. If higher speeds are desired, then the flow path may be closed off at the maximum Mach number for scramjet

operation, thrust then being provided by conventional rockets.

As one can imagine, the technical difficulties associated with making such an engine concept a reality are enormous. One of the key areas that must be addressed is the design of the engine intake. The study described in the current paper examined the performance of a proposed RBCC inlet at a point in the vehicle trajectory when flow is at Mach 4 at the inlet face. The engine will typically operate in ramjet mode at this point, hence inlet back-pressure requirements are high. The most important properties of the interest in the study were the starting characteristics of the inlet, the mass capture and the maximum back-pressure the inlet could withstand. These were all determined during the experiments. The computational portion of the investigation provided confirmation of the mass capture obtained in the experiments, along with the details of the overall flow structure within the inlet. The computations also provided information on aspects of the efficiency and performance of the inlet which were not obtained in the experiments.

Experimental Program

Wind Tunnel Test Conditions and Instrumentation

The experiments were conducted at NASA Langley Research Center in the Mach 4 Blown Down Facility (M4BDF). Typical operating conditions were a Mach number of 4.03, a stagnation pressure of 1.38 Mpa (200 psia), a stagnation temperature of 290 K (522° R), and a Reynolds number of 6.1×10^6/m (20×10^6/ft). The M4BDF has a 22.9cm x 22.9cm (9in. x 9in.) test section which is 0.91m (3ft) in length. Diagnostic instrumentation for the tests included approximately 50 surface pressure taps, a thermocouple to determine the model wall temperature, and a turbine flow meter to measure the bleed mass flow. The mass flow rate through the inlet was determined using a sonic throat based flow metering device. All data was acquired and saved using a PC based data acquisition system. A Schlieren system was installed to obtain images of the external flow past the inlet. Typical runs lasted approximately 2 minutes.

Experimental Model

A photograph of the fully assembled experimental model mounted in the M4BDF is shown in Fig.1. The inlet was a 35% scaled replica of the Rocketdyne Engine A5 inlet configuration developed for the NASA MSFC Advanced Reusable Technology (ART) Program. This fixed geometry inlet had highly swept leading edges, both side-wall and body-side compression, and a constant area isolator. Body-side bleed holes were situated a short distance downstream of the inlet throat. Two cowl geometries were tested. In addition, the inlet was tested with and without a 12 in. plate mounted upstream of the model, to gauge its ability to ingest a fore-body boundary layer. Turbulent boundary layer calculations indicated that this plate produced a boundary layer with $\delta / h_{cowl} = 0.074$ and $\delta^* / h_{cowl} = 0.030$ for the tests with the forebody plate. Body-side and cowl pressure taps were on the symmetry plane of the model. The side-wall taps were concentrated on one side of the model, and were situated along lines at 15%, 50% and 85% of the height of the side walls. The model exhausted directly into a rectangular flow metering device which was approximately 46 cm (18 in.) in length. Back-pressure was applied to the inlet by varying the throat height of the flow meter through the movement of a horizontal flap. Typical runs involved exposing the inlet to an increasing back-pressure until it unstarted; and then reducing the back-pressure to ascertain whether a particular configuration would self-start. The error associated with the inlet mass capture measurements was approximately +/- 2.3% of $\dot{m}_{base}$.

Figure 2 shows the cowl configurations utilized in the tests. Figure 2(a) shows the notched cowl, which had a 20° notch centered on the symmetry plane of the inlet and a leading edge included angle of 15°. Figure 2(b) shows the straight cowl, which also had a leading edge included angle of 15°. Both cowls, and all side walls, had sharp leading edges. The axial position of each cowl was adjustable. Four different body-side bleed plates were fabricated for the tests. These plates were installed flush with the body-side surface of the isolator, just downstream of the throat. One was blank (no bleed), while the remaining three had a series of 0.1 in. diameter bleed holes. Each of these plates had the same bleed hole pattern, but had the holes slanted

downstream at different angles relative to the normal to the isolator surface. Slant angles of 30°, 45° and 70° were fabricated (Fig. 3 shows a drawing of the 45° bleed plate). The higher the slant angle relative to the normal to the isolator surface, the larger the expected bleed through the plate.

Bleed Measurement System

In the current configuration the air bled from the body-side of the model flowed into a cavity below the inlet isolator, passed through a series of tubes and the turbine flow meter, and then exhausted back into the wind tunnel test section downstream of the model. The turbine flow meter was an EG&G Flow Technology Inc. model FT-16 with a maximum volumetric flow rate of 50 SCFM. Frequency output from the flow meter was converted to voltage using a Pioneer Magnetics Inc model PM1870 converter. Measurement of the temperature and the pressure of the bleed flow adjacent to the flow meter enabled the bleed mass flow rate to be determined. The error associated with bleed flow rates included in this paper was approximately +/- 0.02% of $\dot{m}_{base}$.

Table 1 shows the measured bleed levels for the three different bleed plates, both in the absence of back-pressure and also with the large back-pressure that occurred during restart. In general, $m_{bl} = \dot{m}_{bl} / \dot{m}_{base}$ was at its highest level during the period between unstart and restart, and peaked just before restart. Note that in the absence of back-pressure, m_{bl} increased with hole slant angle, as expected. At restart, however, m_{bl} was similar for all three bleed plates. This indicated that losses within the bleed measurement system were limiting m_{bl}. Attempts to increase m_{bl} by reducing bleed measurement system losses were unsuccessful.

Experimental Results

A total of 101 runs were performed during the test program. Table 2 lists all the tested configurations and the designations used to describe them in this paper. For each configuration, tests were performed to determine the most forward cowl position at which the inlet would start. This cowl position was considered to produce the maximum performance for a particular configuration.

The experimental results are described in four sub-sections; each section associated with a different aspect of the acquired inlet data. These are:

(A) Surface pressure distributions.
(B) Inlet mass capture.
(C) Maximum back-pressure.
(D) Starting characteristics.

Sub-section (E) contains a description of the optimum inlet geometry which and a statement of its measured performance.

(A) Surface Pressure Distributions

The surface pressure distributions measured during the tests supplied information on many features of the inlet flowfield. Figure 4 shows typical pressure distributions on the body, side-walls and cowl of the model, when operating with no back-pressure. Body-side pressure level increased gradually to a peak of $p/p_{ref} = 2.1$ at the throat, followed by a decrease along the isolator. The side wall pressure distributions had similar shape up to the throat, however the 50% and 85% line pressures did not decrease in the isolator, due to the influence of the cowl shock. Cowl pressures were significantly higher than the body-side levels (varying between $p/p_{ref} = 3.2$ and 4.8), due to the significant flow turning generated by the cowl shock. Side-wall pressure levels in the isolator showed the influence of the cowl shock, which struck the body downstream of the isolator exit for most of the tested configurations.

Typical body-side pressure distributions measured at different times during a test; i.e. with different back-pressure levels, are shown in Fig. 5. These include the body-side pressure distribution with no back-pressure; the pressure distribution corresponding to the maximum back-pressure with no disturbance upstream of the throat (t = 77 sec); the pressure distribution corresponding to the maximum back-pressure (t = 78 sec); the unstarted pressure distribution (t = 79 sec); and a typical pressure distribution after the inlet had restarted (t = 97 sec). For some configurations, the maximum back-pressure sustained by the inlet was up to 15% higher than the maximum back-pressure with no disturbance upstream of the throat. Pressure data such as that shown in Fig. 5, along with schlieren images of the inlet flowfield, indicated that the unstarted flowfield produced disturbances that propagated forward to the leading edge of the inlet.

(B) Inlet Mass Capture

Inlet mass capture ($\dot{m}_{cap}$) was determined by the use of the flow metering device. Assuming no heat transfer to the model, and sonic flow at the throat of the flow meter, $\dot{m}_{cap}$ was calculated as follows:

$$\dot{m}_{cap} = \left(\frac{(\gamma+1)}{2}\right)^{\frac{-(\gamma+1)}{2(\gamma-1)}} p_t \sqrt{\frac{\gamma}{RT_t}} A_{fm} \quad (1)$$

Figure 6 shows the variation of the mass capture ratio, $m_c = \dot{m}_{cap} / \dot{m}_{base}$, throughout a typical run, along with the flow meter throat area (A_{fm}). Note that the base-line mass flow, $\dot{m}_{base}$, is the mass capture of the straight cowl configuration with the cowl leading edge at the throat and no forebody plate. At the beginning of the run A_{fm} was fully open and the flow was not sonic at the flow meter throat, so equation (1) is not accurate. By t = 55 sec. the inlet was highly back-pressured, flow was choked at the flow meter throat, and equation (1) supplied a reliable measure of $\dot{m}_{cap}$. Unstart occurred in the run shown in Fig. 6 at t = 71 sec., as indicated by the drop in m_c. Note, however, that m_c began to slowly decrease before unstart; i.e. the inlet spilled before it unstarted. Throughout the test program it was observed that inlet spillage corresponded with the periods in which disturbances occurred upstream of the throat. Inlet restart is indicated in Fig. 6 at t = 82 sec. when m_c has returned to its pre-unstart level. The variation in model wall temperature ratio (T_w/T_t) is also plotted in Fig. 6. Note that T_w/T_t remained constant throughout the run and was very close to the adiabatic wall temperature for a turbulent boundary layer at Mach 4.

Figure 7 shows m_c for all the configurations which exhibited the ability to restart in the testing program. In order to make a fair comparison between the two cowl geometries, m_c is plotted versus A_{cov}/A_{tot}, where A_{cov} is the coverage area of the cowl upstream of the inlet throat, and A_{tot} is the total spill area of the inlet upstream of the throat. From an examination of Fig. 7 it is clear that the notched cowl had superior mass capture relative to the straight cowl for the same A_{cov}/A_{tot} at all values of A_{cov}/A_{tot} and for both forebody plate lengths, by approximately 1.5 %. It is also clear that the notched cowl allowed starting of the inlet with larger A_{cov}/A_{tot}. Note that above $A_{cov}/A_{tot} = 0.1$, the increase in m_c began to flatten out, indicating that movement of the cowl further forward than positions corresponding to $A_{cov}/A_{tot} = 0.1$ does not increase m_c at as fast a rate as that observed below $A_{cov}/A_{tot} = 0.1$. Table 3 lists the maximum m_c measured for each inlet configuration.

(C) Maximum Back-Pressure

The results presented in this sub-section concentrate on the maximum back-pressure achieved by the inlet before disturbances were observed to move upstream of the throat (p_{max}). Data showing the maximum back-pressure achieved by the inlet, regardless of whether disturbances moved forward of the throat, (p_{max_d}), is discussed at the end of this sub-section. In the current paper, the back-pressure imposed on the inlet is assumed to be equal to the body-side surface pressure at the exit of the isolator.

Figure 8 shows the maximum back-pressure ratio (p_{max}/p_{ref}) for all tested configurations. In general, maximum back-pressure was not found to depend on A_{cov}/A_{tot} (i.e. cowl position), or cowl geometry, and p_{max}/p_{ref} varied between 4.5 and 5.4 for almost all inlet configurations. The higher p_{max}/p_{ref} levels corresponded to configurations with body-side bleed and no forebody plate.

As previously noted, all the bleed configurations removed similar amounts of air when the inlet was highly back-pressured. The effect of both the 30° and 45° bleed plates was to increase maximum back-pressure by 8-12% over no bleed levels. However, the 70° bleed plate showed no improvement over the no-bleed cases. It is believed that the ineffectiveness of the 70° bleed plate was related to the mismatch between the maximum amount of bleed possible with this plate, and the mass flow limit of the bleed measurement system. This mismatch led to an elevated pressure in the bleed flow cavity and some interaction with the isolator which reduced the effectiveness of the bleed. The presence of a forebody boundary layer with $\delta^*/h_{cowl} = 0.03$ reduced p_{max}/p_{ref} by only 5-8% for all tested configurations. This relative insensitivity of the inlet back-pressure performance to a sizable ingested boundary layer indicated that this inlet is

a good candidate for airframe integrated engine configurations.

Figure 9 shows the maximum back-pressure ratio for all tested configurations, regardless of the presence of disturbances upstream of the throat (p_{max_d}/p_{ref}). This ratio ranged between 4.5 and 6.2, and for some configurations, p_{max_d}/p_{ref} was up to 15% higher than p_{max}/p_{ref}. For these configurations, increase of back-pressure above p_{max}/p_{ref} led to a stable, intermediate flow structure with some level of body-side pressurization upstream of the throat. For other configurations, increase of back-pressure above p_{max}/p_{ref} immediately led to unstart. As already discussed, tests which showed differences between p_{max}/p_{ref} and p_{max_d}/p_{ref} also appeared to spill before unstart. Due to the scatter in the data, the dominant parameter effecting the variation between p_{max}/p_{ref} and p_{max_d}/p_{ref} was not able to be clearly identified.

(D) Starting Characteristics

In this paper an inlet is referred to as self-starting if it restarted after the removal of back-pressure. The starting limit of a particular inlet configuration was the most forward cowl position for which the inlet self-started. Figure 10 shows the self-starting limits for the four tested combinations of cowl geometry and forebody plate length on a graph of bleed magnitude versus A_{cov}/A_{tot} (i.e. cowl position). For all configurations, increased bleed level enabled the inlet to self-start with the cowl moved forward. For the same bleed level, the notched cowl started at a larger A_{cov}/A_{tot}. The presence of the forebody plate reduced the starting A_{cov}/A_{tot} for a particular bleed level. Finally, introduction of the cowl relief slot considerably increased the starting A_{cov}/A_{tot} for the notched cowl from A_{cov}/A_{tot} = 0.11 to 0.15.

Table 4 lists the cowl position, m_c and A_{cov}/A_{tot} corresponding to the self-starting limit for each combination of cowl geometry and forebody plate length. Both the no-bleed and 45° bleed plate values are shown. The cowl position, x_c/x_{th}, is the normalized distance upstream of the throat of the leading edge of the straight cowl, or the crotch of the notched cowl.

(E) Optimum Inlet Configuration

Within the parameter limits of the current test program, the best inlet performance, in terms of mass capture and maximum back-pressure, was achieved with the following configuration:

- 20° notched cowl.
- cowl relief slot.
- 1.5% body-side bleed.

Peak mass capture was m_c = 108.9 and 112.5% with and without the forebody plate, respectively. Maximum back-pressure was p_{max}/p_{ref} = 5.0 and 5.4 with and without the forebody plate, respectively.

Computational Analysis

Computational analysis of a subset of the tested inlet configurations was conducted to supplement the experimental data. The NASA Langley code VULCAN[1] was used to solve the inlet flowfield on typical grids with between 2.0 and 3.0 million grid points. These computations were limited to cases without bleed or back-pressure, and assumed turbulent flow throughout with adiabatic wall conditions. Both the external flow past the inlet and the internal flow through the inlet were solved.

VULCAN CFD Code

VULCAN[1] is a 3-D, upwind, viscous, compressible code, for structured multi-block grids, with a full range of turbulence models. For the current computations the air was assumed to be a perfect gas with γ = 1.4 and a $k-\omega$ turbulence model with a Boussinesq Reynolds stress model was chosen. The computations also made use of wall functions to reduce the size of grids. Depending on the cowl geometry and the presence of the forebody plate, the grid topology contained between 30 and 40 blocks. The computations were performed on a DEC Alpha 21164 machine. The CPU time required for the solutions ranged between 45 and 60 hours.

Grid Topology

The swept leading edges and notched cowl of the inlet geometry posed some interesting problems for the generation of a suitable computational grid. While the VULCAN[1] code can be run with grids containing singularities, solution convergence is always a problem in these areas, particularly when the surrounding flow structure is complicated. This fact led to the use of a grid topology which kept block boundaries on

the leading edges, but contained no singularities. Figure 11 shows a close up view of a typical leading edge grid topology used in the current inlet grid. The singularity has been removed from the apex of the leading edge, and the block boundary follows the swept leading edge. The only difficulty associated with this topology is that space-marching the solution is not possible, hence an elliptic flow solver must be used in regions which contain this grid topology. Figure 12 shows a schematic of the grid blocking structure used in the computation. The flowfield was solved in 8 separate regions. Regions 2,4 and 7 were solved space-marching; whereas regions 1,3,5,6 and 8 were solved elliptically. Regions 1,3 and 6 contained blocks which utilized the grid topology shown in Figure 11.

Computational Results

The experimental configurations that were computationally analyzed are listed in Table 5. Two no-bleed cases were performed for each cowl geometry; one case with and one case without the forebody plate. The cowl positions chosen for the calculations corresponded with the self-starting limit of each cowl with maximum bleed and the forebody plate installed (see Table 4).

Figure 13 shows an isometric view of a typical calculated flowfield with Mach number contours shown on a number of axial planes. Flow is attached to the swept side leading edges and the external flow above the inlet is dominated by vortical structures that form at the top of the side-walls. The characteristic bulge in the body-side boundary layer (caused by the swept shocks from the side walls) can also be seen near the symmetry plane of the model.

Figures 14(a) and (b) show the symmetry plane Mach number contours for cases S_A and N_A respectively. Both flowfields are identical upstream of the cowl region, and clearly show the body-side shock attached to the leading edge of the inlet. This shock becomes steeper as it merges with the side-wall shocks and passes above the inlet well upstream of the cowl. In the straight cowl flowfield (Fig. 14(a)) the cowl shock is attached to the cowl leading edge and propagates towards the body-side, striking the body just downstream of the isolator exit. Some separation of the body-side and cowl boundary layers occur near the end of the computational domain as a result of the recompression shocks generated by the closure of the recirculation regions behind the back-ward facing steps at the isolator exit. In the notched cowl flowfield (Fig. 14(b)), the cowl shock is not attached at the crotch of the cowl. This is caused by the high sweep of the cowl leading edges. Cowl shock detachment is not a desirable feature in this inlet, as this increases flow spillage and local heating. It also means that the cowl shock strikes the body-side of the inlet further upstream than an attached cowl shock, as indicated by the fact that even though the leading edge of the straight cowl of Fig. 14(a) is upstream of the cowl crotch of Fig. 14(b), the cowl shock of Fig. 14(b) strikes the body-side earlier. Reduction of the cowl leading edge sweep angle could remove this feature of the flowfield.

Comparison with Experiments

The computational results have been compared with the experimental measurements in terms of the inlet mass capture and the surface pressure distributions on the cowl and body-side of the model. Table 6 shows m_c for all the computations together with m_c for the corresponding experimental configurations (based on the curves through the data plotted in Fig. 7). The CFD indicates a slightly higher m_c than the flow meter measurements by an amount that is within the estimated experimental error of +/- 2.3% of $\dot{m}_{base}$, for all cases. These results therefore supply a satisfying confirmation of the accuracy of the flow meter. The maximum m_c of 1.123 was calculated for the notched cowl with no forebody plate (case N_A).

Figure 15(a) and (b) show an experimental/computational comparison of the symmetry plane cowl and body-side pressure distributions, along with a contour plot of the calculated body-side pressure distribution for cases N_A and N_B. Both the body-side and cowl pressure levels measured on the inlet symmetry plane appear to be well predicted by the CFD. The computations are therefore expected to contain all the dominant features of the flowfield. Slight under prediction of the body-side pressure leading up to the throat, and slight over prediction in the isolator were the major difference between the experimental and computational results. The body-side pressure contours show that the body-side pressure is fairly uniform across the inlet in the throat region, and clearly show the position where the cowl shock reaches the body and some detail of the expansion and re-compression wave structures that occurs in the combustor.

One-Dimensional Properties at the Isolator Exit

The equivalent one-dimensional properties at the isolator exit have been calculated from the computations. The mass flow averaged total pressure recovery (P_T), process efficiency (η_{KD}) and kinetic energy efficiency (η_{KE}) for all computational cases are listed in Table 7. The notched cowl generated flows with higher performance and efficiency than the straight cowl. The introduction of the forebody plate reduced the total pressure recovery of both cowl geometries by approximately 4%.

Conclusions

- 101 tests of a 35% scale model of an RBCC inlet were completed at $M_1 = 4.03$, $Re_1 = 20 \times 10^6$/ft and adiabatic wall conditions.
- Inlet mass capture ranged between 97.3 and 112.5% of the base-line mass flow. These values were confirmed by the CFD calculations.
- The maximum back-pressure to reference pressure ratio (with no disturbances upstream of the throat) ranged between 4.46 and 5.41 for all tested configurations.
- For some configurations a higher back-pressure was achieved with disturbances upstream of the throat. Maximum back-pressure to reference pressure ratio's up to 6.21 were observed.
- Body-side bleed of 0.93-1.55% of the base-line mass flow increased inlet back-pressure by 8-12% and enabled the inlet to self-start with the cowl further forward.
- Introduction of a 12 in. forebody plate ahead of the inlet (producing a boundary layer with displacement thickness approximately 3% of the cowl height), reduced maximum back-pressure by only 5-8%. This result suggests that this inlet is suitable for airframe integrated engine configurations.
- Introduction of a relief slot in the cowl enabled the inlet to self-start with the cowl further forward.
- The inlet configuration with the best experimental performance included a 20° notched cowl, a cowl relief slot, and body-side bleed of 1.5% of the base-line mass flow. CFD calculations also indicated that the 20° notched cowl was more efficient than a straight cowl.
- CFD calculations predicted the body-side and cowl pressure distributions on the symmetry plane with reasonable accuracy. The computations were therefore expected to contain all the dominant features of the inlet flowfield.
- CFD calculations indicated that the cowl shock was not attached at the crotch of the notched cowl. This may lead to local heating problems. Increased notch angle (i.e. decreased cowl sweep angle) could alleviate this problem.

References

[1] White, J.A., and Morrison, J.H., "A pseudo-temporal multi-grid relaxation scheme for solving the parabolized Navier-Stokes equations", AIAA Paper 99-3360, 14th AIAA Computational Fluid Dynamics Conference, Norfolk VA, June 1999.

Acknowledgement

The authors wish to thank Jeff White of the Hypersonic Airbreathing Propulsion Branch at NASA Langley for his considerable help with the computations. The assistance of NASA Co-ops Brian Tews and Joe Gasbarre was also appreciated. This work was funded by NASA MSFC and NASA LaRC.

Bleed Plate	m_{bl} (%) No back-pressure	m_{bl} (%) Restart (high back-pressure)
30° holes	0.33 – 0.35	0.96 – 1.26
45° holes	0.41 – 0.52	0.93 – 1.55
70° holes	0.61 – 0.73	0.88 – 1.29

Table 1 - Body-side bleed levels.

Designation	Cowl Geometry	Forebody Plate Length (in.)	Bleed Configuration
S-0-N	straight	0.0	None
S-0-45	straight	0.0	45° holes
S-12-N	straight	12.0	none
S-12-45	straight	12.0	45° holes
N-0-N	notched	0.0	none
N-0-30	notched	0.0	30° holes
N-0-45	notched	0.0	45° holes
N-0-70	notched	0.0	70° holes
N-12-N	notched	12.0	none
N-12-45	notched	12.0	45 ° holes
N-12-70	notched	12.0	70° holes
NR-0-45	notched /relief slot	0.0	45 ° holes
NR-12-45	notched /relief slot	12.0	45 ° holes

Table 2 - Designations of tested inlet configurations.

Configuration	Maximum m_c (+/- 2.3%)
S-0-(N,45)	1.079
S-12-(N,45)	1.057
N-0-(N,30,45,70)	1.125
N-12-(N,45,70)	1.087
NR-0-45	1.125
NR-12-45	1.082

Table 3 – Maximum m_c for different configurations.

Configuration	x_c/x_{th}	m_c **(+/- 2.3%)**	A_{cov}/A_{tot}
S-0-N	0.066	1.082	0.059
S-0-45	0.085	1.070	0.080
S-12-N	0.057	1.010	0.049
S-12-45	0.066	1.051	0.059
N-0-N	0.038	1.100	0.073
N-0-45	0.066	1.127	0.109
N-12-N	0.028	1.069	0.062
N-12-45	0.047	1.069	0.084
NR-0-45	0.095	1.118	0.149
NR-12-45	0.057	1.075	0.092

Table 4 - Inlet self-starting limits.

Computational Designation	Experimental Designation	Cowl Position x_c/x_{th}
S_A	S-0-N	0.066
S_B	S-12-N	0.066
N_A	N-0-N	0.047
N_B	N-12-N	0.047

Table 5 - Designations of CFD Analysis Cases.

Computational Designation	m_c CFD	m_c (+/- 2.3%) experiment
S_A	1.092	1.067
S_B	1.049	1.044
N_A	1.123	1.102
N_B	1.092	1.081

Table 6 - Comparison of computational and experimental mass capture.

Computational Designation	P_T	η_{KD}	η_{KE}
S_A	0.750	0.914	0.974
S_B	0.719	0.904	0.970
N_A	0.761	0.920	0.975
N_B	0.729	0.909	0.971

Table 7 Equivalent one-dimensional efficiency parameters at the isolator exit.

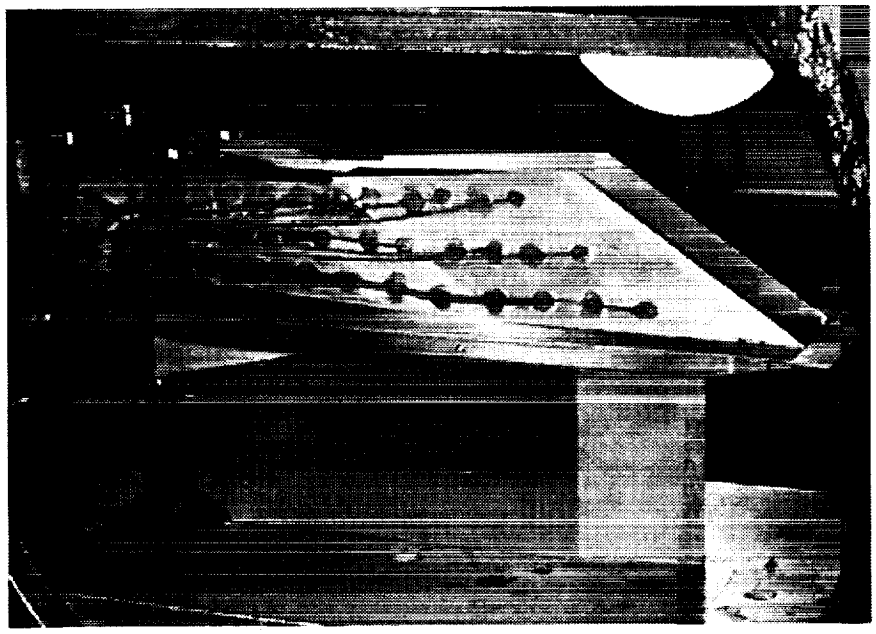

Figure 1 - Photograph of Inlet model in the wind tunnel.

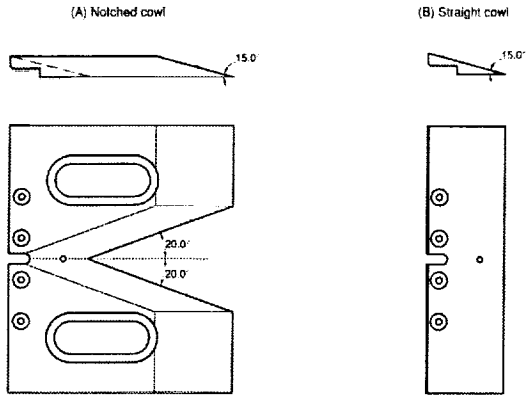

Figure 2 - Cowl Geometries

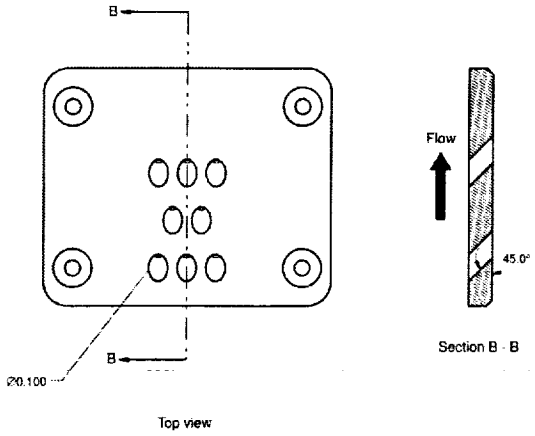

Figure 3 - Bleed Plate Geometry

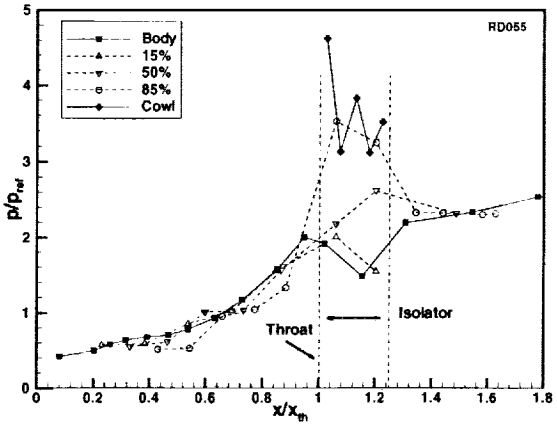

Figure 4 - Surface pressure distributions with no back-pressure.

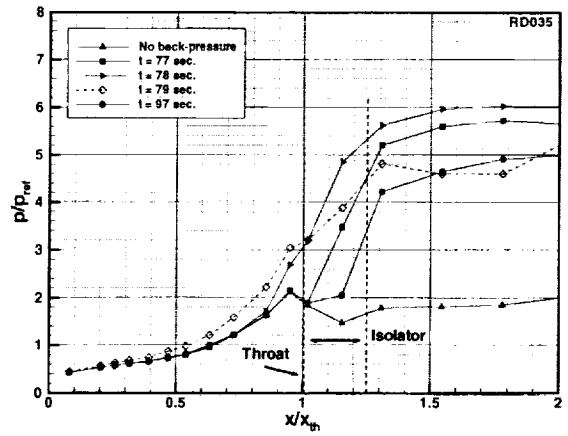

Figure 5 - Body-side pressure distributions at different times during a run.

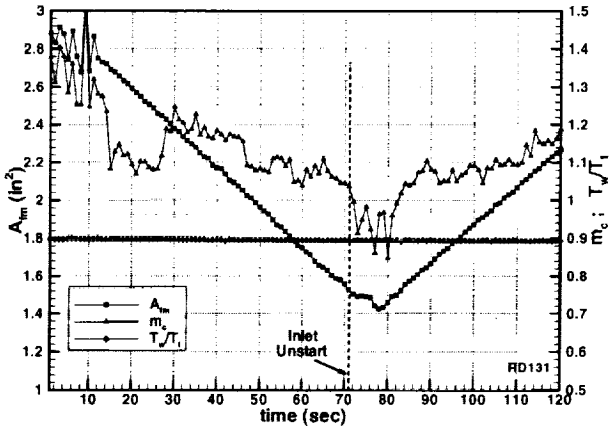

Figure 6 - Inlet mass capture and wall temperature variation during a run.

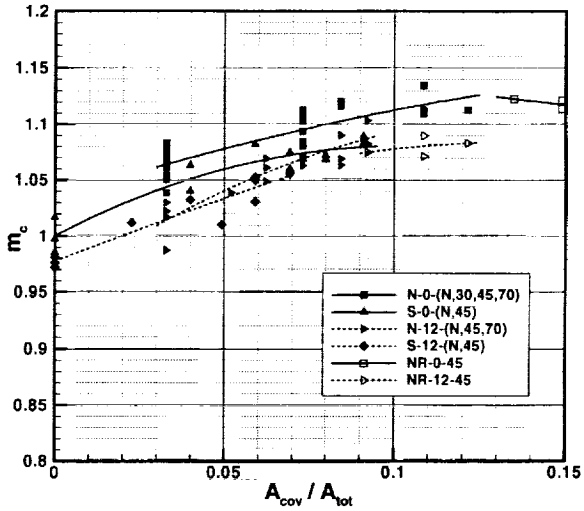

Figure 7 - Mass capture for all configurations.

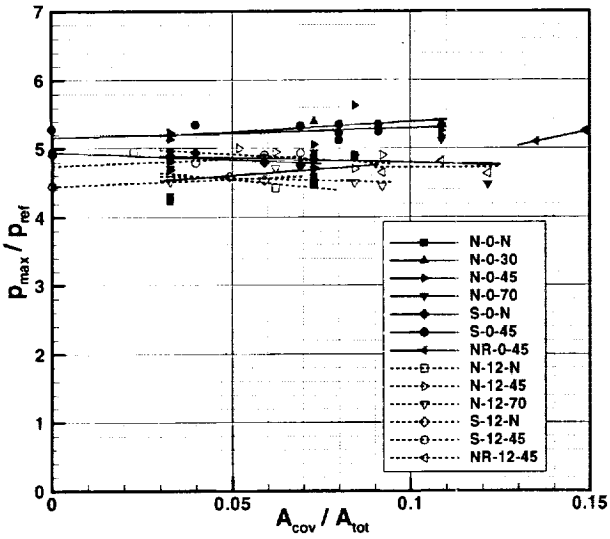

Figure 8 - Maximum back-pressure with no disturbances upstream of the throat for all configurations.

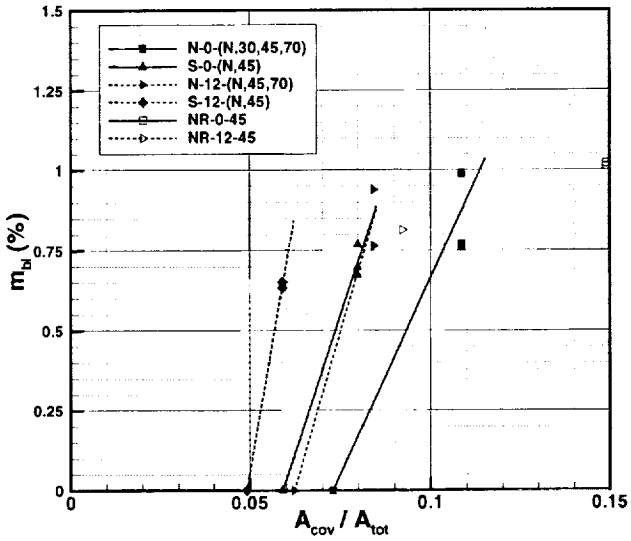

Figure 10 - Self-starting limits for all configurations.

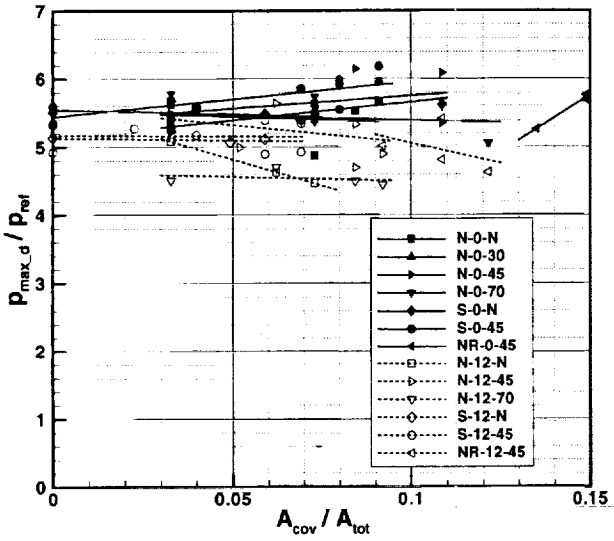

Figure 9 - Maximum back-pressure for all configurations.

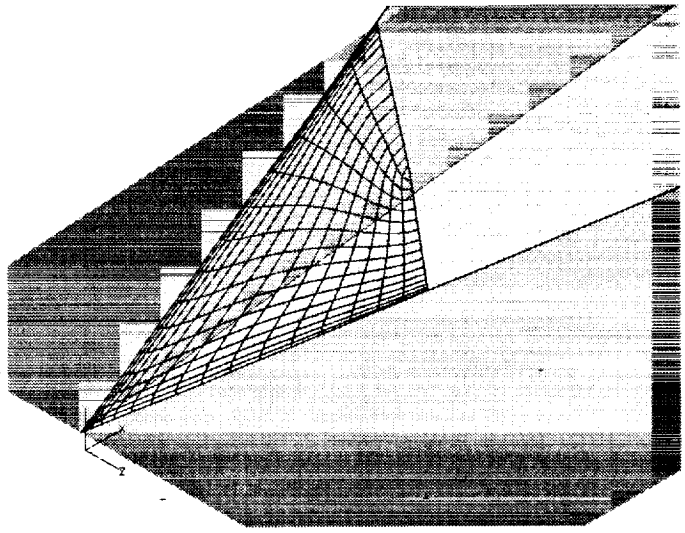

Figure 11 - Grid topology used with swept leading edges.

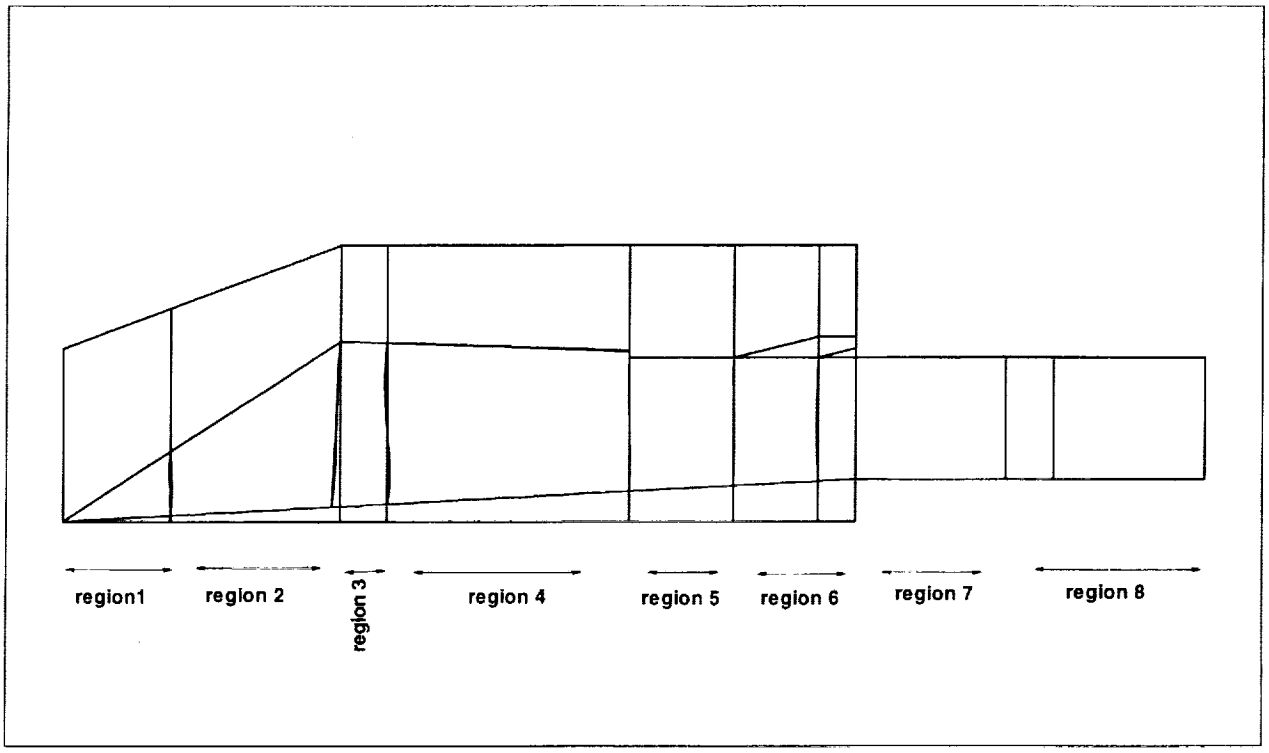

Figure 12 - Schematic of regions used for flow solution (not to scale).

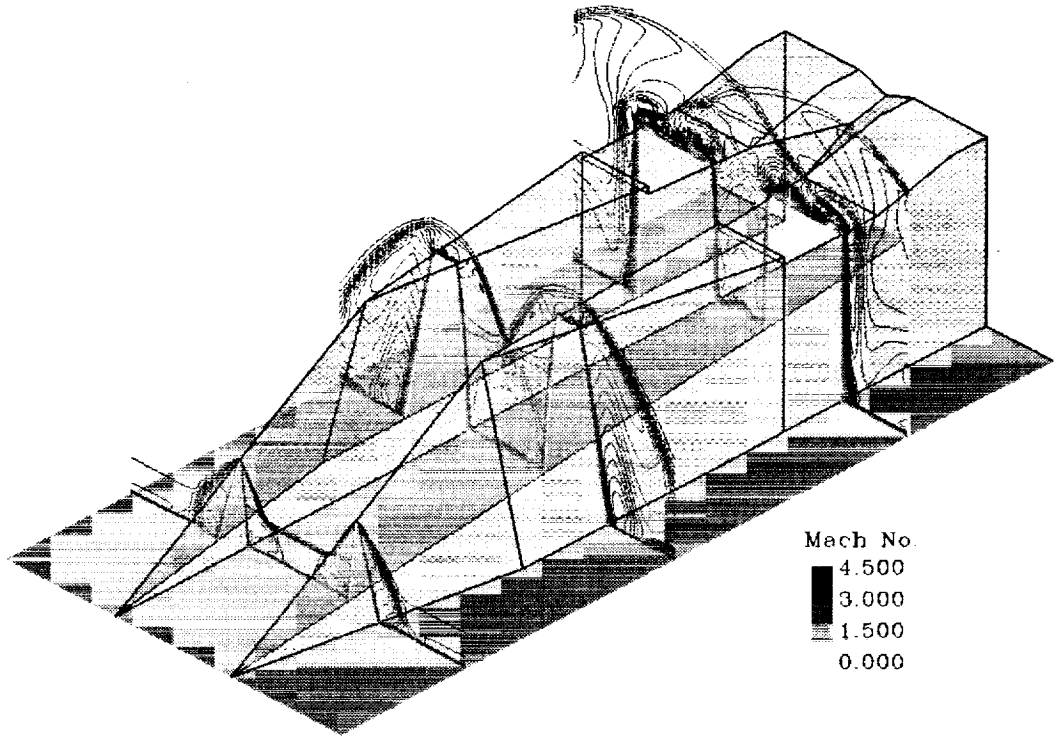

Figure 13 - Isometric view of inlet flowfield showing Mach number contours (not to scale).

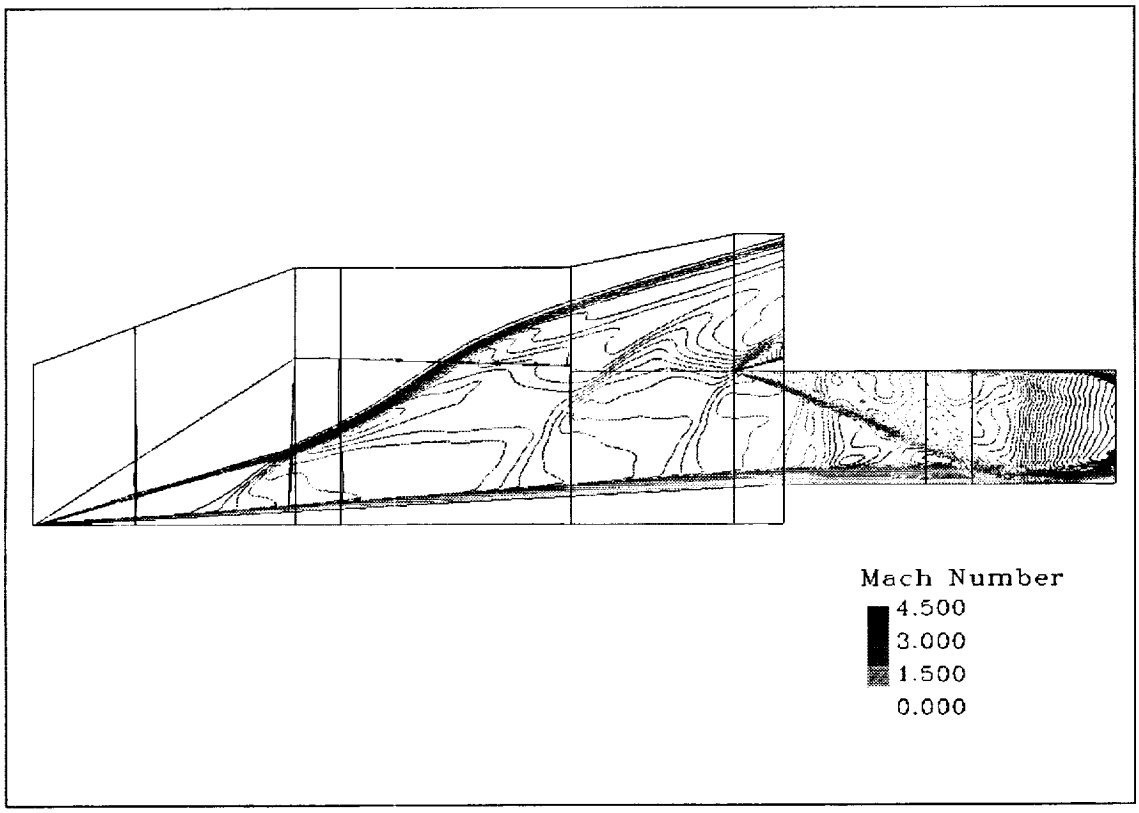

Figure 14(a) - Symmetry plane Mach number contour for case S_A (not to scale).

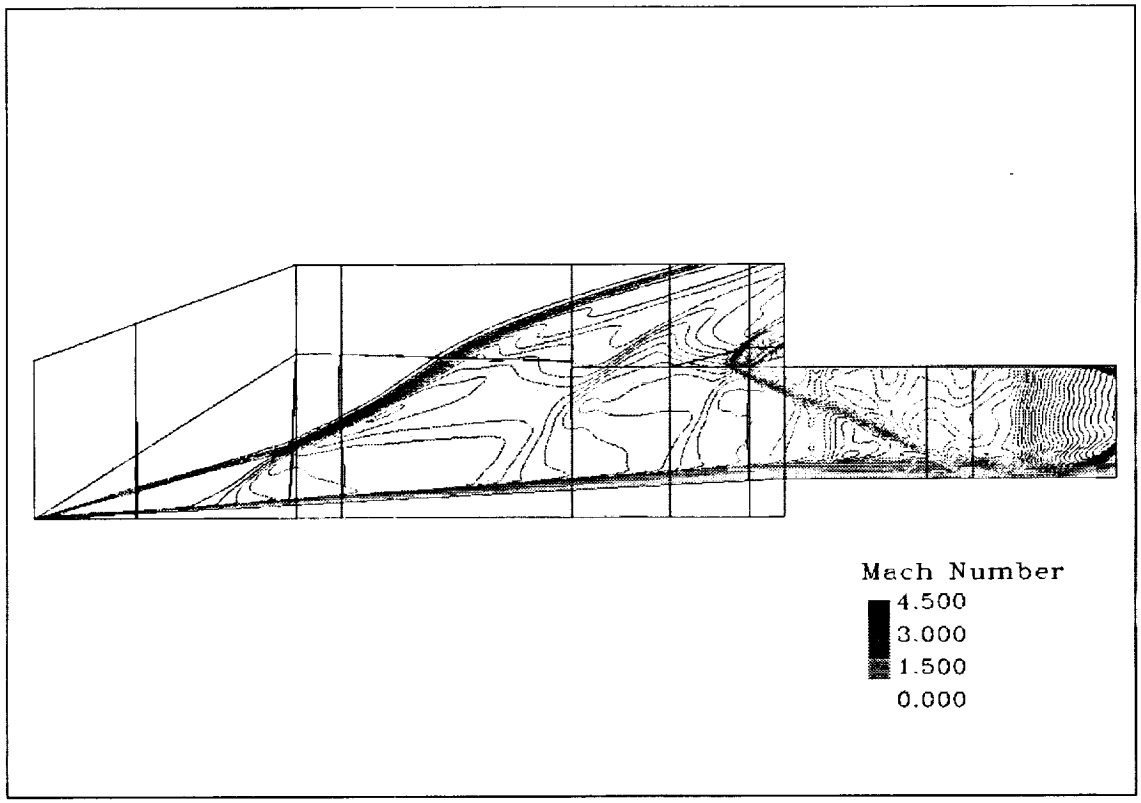

Figure 14(b) - Symmetry plane Mach number contour for case N_A (not to scale).

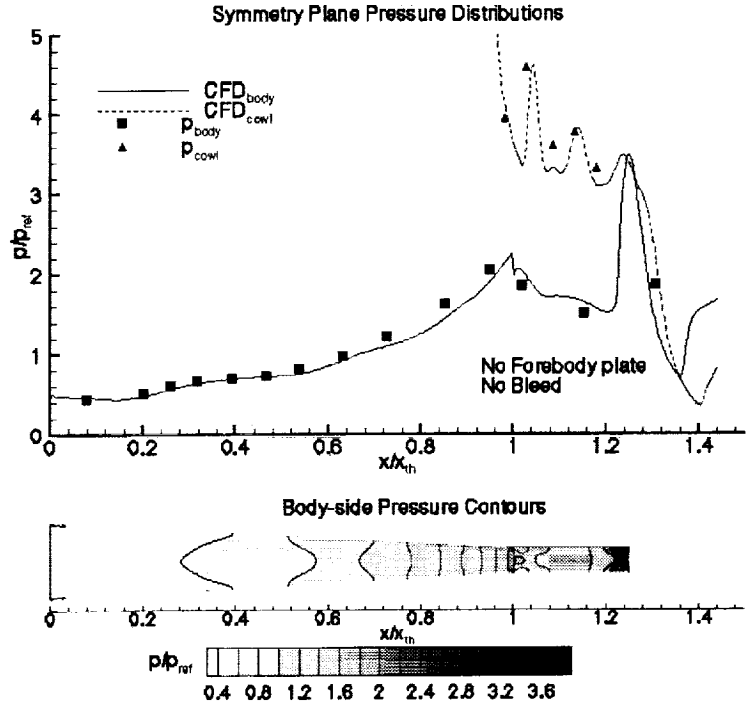

Figure 15(a) - CFD/Experimental Comparison for case N_A.

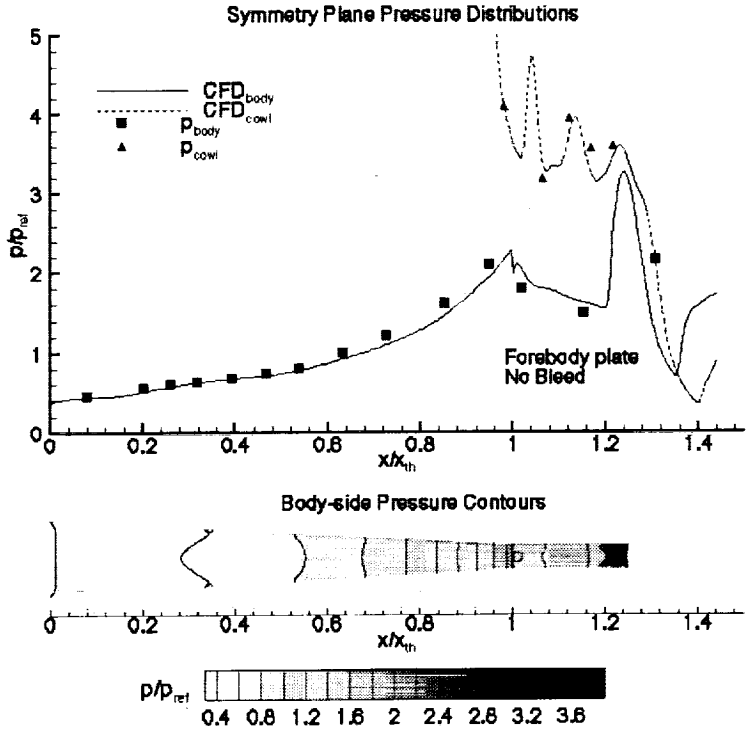

Figure 15(b) - CFD/Experimental Comparison for case N_B.